Contents lists available at ScienceDirect

Journal of Quantitative Spectroscopy & Radiative Transfer

Light transport with the equation of radiative transfer: The Fourier Continuation – Discrete Ordinates (FC–DOM) Method

E.L. Gaggioli [a,b,*], O.P. Bruno [c], D.M. Mitnik [a,b]

[a] *Instituto de Astronomía y Física del Espacio (IAFE, CONICET–UBA), Casilla de Correo 67 - Suc. 28 Buenos Aires, (C1428ZAA), Argentina*
[b] *FCEyN, Universidad de Buenos Aires, Argentina*
[c] *Computing and Mathematical Sciences, Caltech, Pasadena, CA 91125, USA*

ARTICLE INFO

ABSTRACT

We present a method for the treatment of the time dependent radiative transfer equation under the discrete ordinate approximation. The novelty of the proposed approach stems, in part, from the incorporation of a spectral method for the calculation of the spatial differential operators based on the Fourier Continuation procedure introduced recently by Bruno and co–authors. This is a spatially dispersionless and high order method, which can handle arbitrary geometries, including those encountered in the forward model of light transport in optical tomography. We validate our theoretical results by comparison with analytic and experimental outcomes of the fluence measurements on tissue-like phantoms. The method makes it possible to calculate the time of flight of photons in random media efficiently and with high accuracy.

1. Introduction

Neutral particle transport modelling is of interest on many branches of science and technology. Applications include radiation transport in planetary and stellar atmospheres [1], remote sensing [2,3], neutron transport research for nuclear reactor design [4,5], radiation heat transfer for industrial applications [6], and modeling of transport of photons in tissue–like media for medical physics applications [7–9] among others. In this paper we are particularly concerned with optical tomography applications where the main goal is characterization of biological media on the basis of light measurements typically involving external illumination. The biological body could be a human breast or neck (for applications in tumor diagnosis [10,11]), a head (where the information of the transmitted and diffusely reflected light provides functional information of the brain through the characterization of the blood flow and the oxygenation state of hemoglobin [12]), or a finger (with applications in the diagnosis of finger joint arthritis, among others [13]). Infrared light, which can penetrate and sense several centimeters within tissue, is mostly used in these contexts. Light is detected at different locations in reflection or transmission configurations. In order to infer the optical properties of the media, iterative reconstruction techniques need accurate results in a very

short amount of time. With this goal in mind, we have developed the present method.

The governing equation for neutral particle transport is known as the radiative transfer equation or the neutron transport equation, depending on the field of application. This equation is the linearized Boltzmann equation, which is formulated in phase space. It models the transport of particles which interact mainly with a background media, and do not interact with each other. The radiative transfer equation (RTE) comprises a multidimensional problem even for simple cases in one spatial dimension, because it involves both the position and the velocity domains, in addition to time. In view of the importance and wide applicability of this equation, and in view of the high computational complexity it entails, several numerical techniques have been proposed for its treatment, including stochastic and deterministic methods (see, for example [5,14]).

The most widely used stochastic method in radiative transfer is the Monte Carlo method. While quite simple, this approach is computational more demanding than deterministic methods. Among deterministic techniques, the most popular are the P_N method [15] and the discrete ordinates method. In the P_N method the solution is factored into spatial and angular components. The angular component of the specific intensity is expanded in spherical harmonics, yielding a hierarchy of coupled partial differential equations, the lowest-order one of which is a diffusion–like equation. This "diffusion approximation" for photon transport can also be obtained through asymptotic analysis, and it corresponds to a regime

in which the mean free path of the particles is much smaller than the characteristic length of the physical system [16,17], i.e., a highly scattering region.

In the present work we employ the discrete ordinates method (DOM), originally derived by Chandrasekhar [1], who was mainly concerned with astrophysical applications. In the DOM method the angular component is decomposed into a set of discrete directions representing the propagation directions of the rays. The radiation transfer equation becomes a set of equations in a fixed grid, coupled through the collision terms. For the treatment of the spatial differential operator, several techniques have been proposed, including prominently the finite difference method [18,19], the finite element method [20,21], and the finite volume method [22].

In our work, a novel spectral technique developed in [23,24], the Fourier Continuation (Gram) (FC–Gram) method, is employed for the first time to solve radiation transport problems. This approach utilizes an analytical method to continue any given function into a periodic function in an enlarged domain of definition. Hence, Fourier transforms can be employed for the differential operators, thus achieving spatial high order and very small amounts of artificial spatial dispersion.

A major problem concerning the treatment of the RTE is the computation time needed for its solution. The high dimensionality of the transport equation makes its numerical treatment a computationally intensive task. In optical tomography, several iterations over the forward model are required in order to solve the parameter reconstruction problem, posing computationally a tremendously demanding problem. For this reason, approximations to the RTE as the diffusion equation are generally employed. However, the employment of the diffusion equation is not physically accurate in media where absorption dominates, in regions close to the source in optical tomography, or in low scattering regions. The method presented here yields accurate solutions of the transport problem with coarser grids, having a direct impact on the computation time required for a given accuracy.

We tested the accuracy and performance of our method, validating the numerical results with analytical solutions, manufactured problems and experimental results. The FC method can approximate the derivatives of the RTE with fourth–order accuracy, and, as demonstrated in [25], it gives rise to small dispersion errors. The paper is arranged as follows. In Section 2 the main governing equations and boundary conditions for radiative transport are presented, and the physical significance of these equations is discussed. In Section 3 the numerical methods employed and the Fourier Continuation Discrete Ordinates Method (FC–DOM) implementation are described. In Section 4 our results are examined, by comparisons with analytical solutions and detector readings on tissue–like phantoms reported by Klose *et al.* [19]. The first phantom examined is homogeneous, and the second phantom contains a void–like region, giving rise to a situation for which the diffusion equation fails to describe photon-transport correctly. Also in this section, our FC–DOM is compared with another DOM method proposed by Fujii et al. [26], employing a third–order finite difference scheme. A few concluding comments, finally, are presented in Section 5.

2. Light transport model

We employ the radiative transfer equation as a model for light propagation in turbid media, with absorbing and scattering properties. The light specific intensity $I(\mathbf{r}, \hat{\Omega}, t)$, represents the amount of energy irradiated per unit time, per unit area, per unit of solid angle, at a point $\mathbf{r}$, propagating with direction $\hat{\Omega}$, and at time t. It satisfies the corresponding RTE equation:

$$\frac{1}{c} \frac{\partial I(\mathbf{r}, \hat{\Omega}, t)}{\partial t} + \hat{\Omega} \cdot \nabla I(\mathbf{r}, \hat{\Omega}, t) + \mu_t(\mathbf{r}) I(\mathbf{r}, \hat{\Omega}, t)$$
$$= \mu_s(\mathbf{r}) \int_{2\pi} p(\hat{\Omega} \cdot \hat{\Omega}') I(\mathbf{r}, \hat{\Omega}', t) \, d\hat{\Omega}' + q(\mathbf{r}, \hat{\Omega}, t), \tag{1}$$

where the units of I are $W/(m^2\,sr)$. Here c denotes the average speed of light in the medium (the velocity vector of photons is $\vec{v} = c\hat{\Omega}$), and the coefficients μ_a and μ_s are the macroscopic absorption and scattering coefficients, respectively; the total scattering coefficient μ_t is given by $\mu_t = \mu_a + \mu_s$. The macroscopic coefficients can be related to the microscopic coefficients if the constituents of the media, its concentrations and microscopic cross sections are known. The last term of the Eq. (1), q, is an external source function. Usually, it represents a laser beam. In this work we deal only with monochromatic light, so we ignore all wavelength dependence. For the presentation of our computational method, we will deal here only with two–dimensional problems. Therefore, the integration on right hand side of the equation – the inscattering source–, is performed on the unit circle, which defines all the possible propagating directions for a photon. This integral represents all radiant energy scattered by the medium from all directions into the beam. The function p is the phase function which represents the probability for a photon traveling in direction $\hat{\Omega}'$ to be scattered into the beam with direction $\hat{\Omega}$. We employ the empirical phase function introduced by Henyey–Greeinstein [27], widely used in the optical tomography community to model the highly anisotropic nature of scattering in biological tissue:

$$p(\hat{\Omega} \cdot \hat{\Omega}') = \frac{1}{2\pi} \frac{1 - g^2}{(1 + g^2 - 2g\,\hat{\Omega} \cdot \hat{\Omega}')^{3/2}}. \tag{2}$$

In order to ensure conservation of energy, the phase function is normalized [28,29]:

$$\int_{2\pi} p(\hat{\Omega} \cdot \hat{\Omega}') \, d\hat{\Omega}' = 1. \tag{3}$$

Other quantities of interest are the scalar flux, also known as the fluence rate, which accounts for the total intensity radiated at a particular point:

$$\phi(\mathbf{r}, t) = \int_{2\pi} I(\mathbf{r}, \hat{\Omega}, t) \, d\hat{\Omega}. \tag{4}$$

and the photon current:

$$\vec{\mathcal{J}}(\mathbf{r}, \hat{\Omega}, t) = \int_{2\pi} \hat{\Omega} I(\mathbf{r}, \hat{\Omega}, t) \, d\hat{\Omega}. \tag{5}$$

For optical tomography problems, in general, the measurements of radiation are performed by detectors located at the external boundary of the medium. The flux of photons reaching the detectors [30] is given by

$$\mathcal{J}_+(\mathbf{r}_b, t) \equiv \int_{\Gamma_+} \left[1 - f(\hat{\Omega} \cdot \hat{n})\right](\hat{\Omega} \cdot \hat{n}) I(\mathbf{r}_b, \hat{\Omega}, t) \, d\hat{\Omega}, \tag{6}$$

where $\mathbf{r}_b$ is a point at the domain boundary, $\hat{n}$ is the outward normal versor of the surface, and Γ_+ represents the external boundary surface (in which $\hat{\Omega} \cdot \hat{n} > 0$). The reflections at the inner boundary surface Γ_- (where $\hat{\Omega} \cdot \hat{n} < 0$) due to mismatches on the refractive indexes cannot be neglected, and Fresnel boundary conditions have to be used:

$$I(\mathbf{r}_b, \hat{\Omega}, t) = f(\hat{\Omega}_r \cdot \hat{n}) I(\mathbf{r}_b, \hat{\Omega}_r, t) \quad \text{on } \Gamma_-. \tag{7}$$

In Eq. (7) $\hat{\Omega}_r$ is the specularly reflected direction for a beam incident on the inner surface of the medium:

$$\hat{\Omega}_r = \bar{\mathbf{R}} \hat{\Omega}, \tag{8}$$

with reflection matrix $\bar{\mathbf{R}} = \bar{\mathbf{I}} - 2\hat{n}\hat{n}^T$, where $\bar{\mathbf{I}}$ denotes the identity matrix in two dimensions and f represents the Fresnel reflection coefficient for the corresponding direction.

Let n_m and n_a denote the refractive indexes of the body under examination and its surroundings, respectively. From Snell's law $n_m \sin(\theta_i) = n_a \sin(\theta_t)$, the critical angle for total reflection is given by $n_m \sin(\theta_c) = n_a$. The Fresnel coefficient f is given by:

$$f(\hat{\Omega}_r \cdot \hat{n}) = \begin{cases} \frac{1}{2}\left(\frac{\sin^2(\theta_t - \theta_i)}{\sin^2(\theta_t + \theta_i)} + \frac{\tan^2(\theta_t - \theta_i)}{\tan^2(\theta_t + \theta_i)} \right) & \text{if } \theta_i < \theta_c, \\ 1 & \text{if } \theta_i \geq \theta_c. \end{cases}$$

3. Numerical methods

3.1. Discretization of the angular variable

In order to discretize the radiative transfer equation in the angular variable, we employ the discrete ordinates method. A set of M discrete directions $\hat{\Omega}_m = (\xi_m, \eta_m)$ are choosen, where the direction cosines $\xi_m = \hat{x} \cdot \hat{\Omega}_m = \cos(\phi_m)$ and $\eta_m = \hat{y} \cdot \hat{\Omega}_m = \sin(\phi_m)$ represent the projection of the versor along the x and y axis, respectively. We choose to discretize the directions according to the roots of the Chebyshev polynomials:

$$\phi_m = \frac{\pi(2m-1)}{M}. \tag{9}$$

The directions can be computed for the first quadrant only and the remaining directions then be obtained by symmetry. Denoting the discretized intensity as $I_m = I(\mathbf{r}, \hat{\Omega}_m, t)$, the RTE Eq. (1) becomes:

$$\frac{1}{c}\frac{\partial I_m}{\partial t} + \hat{\Omega}_m \cdot \nabla I_m + \mu_t I_m$$
$$= \mu_s \sum_{m'=1}^{M} w_{m'} \, p_{m,m'} \, I_{m'} + q_m, \tag{10}$$

where the Chebyshev quadrature weights are all given by the single value $w_{m'} = 2\pi/M$.

3.2. Discretization of the time variable

For the discretization of the time variable we employ an explicit Forward Euler scheme. The specific intensity at a particular time $t^{n+1} = n\Delta t$ is computed in terms of known quantities from the previous time step t^n. Denoting $I_m^n = I(\mathbf{r}, \hat{\Omega}_m, t^n)$, the time dependent RTE equation is solved propagating the solution with

$$I_m^{n+1} = I_m^n + c\Delta t \left(\mu_s \sum_{m'=1}^{M} w_{m'} \, p_{m,m'} \, I_{m'}^n + q_m^n \right.$$
$$\left. - \hat{\Omega}_m \cdot \nabla I_m^n - \mu_t I_m^n \right), \tag{11}$$

which is a first order approximation for the time derivative.

3.3. Spatial discretization: The FC(Gram) spectral approach

Fourier collocation methods provide high order accuracy, limited dispersion, and mild CFL conditions. Moreover, Fast Fourier Transform, which can be utilized in conjunction with Fourier collocation methods, make it possible to perform calculations in $\mathcal{O}(N \log(N))$ operations, where N is the number of discretization points. However, application of Fourier collocation methods to non periodic functions gives rise to the Gibbs phenomenon and associated severe accuracy degradations.

The Fourier Continuation method (FC) [23] was developed for the spectral treatment of partial differential equations on general domains with arbitrary boundary conditions. The method relies on a continuation procedure, that extends a non periodic function into a periodic one. This enables the use of Fourier transform methods for evaluation of spatial derivatives, giving rise, in the non–periodic context, to the spectral convergence and dispersionless properties

typical of Fourier methods. The continuation procedure selects the correct harmonics in the Fourier series expansion of the functions involved, avoiding Gibbs phenomena related to function discontinuities, while preserving the high order accuracy of the method.

In order to apply the FC procedure to a non periodic function $g(x)$, the function must first be evaluated at a discretized grid of N points, separated by the same distance h:

$$h = \frac{x_{\max} - x_{\min}}{N} = \frac{x_{N+1} - x_1}{N}. \tag{12}$$

The values of the function $g_i = g(x_i)$ define two vectors. One of them, $\mathbf{g}_l$, is constructed with the first d_l points $\mathbf{g}_l = [g_1, g_2, \ldots, g_{d_l}]^T$, and the other, $\mathbf{g}_r$, with the last d_r points $\mathbf{g}_r = [g_{N+1-d_r}, g_{N-d_r}, \ldots, g_{N+1}]^T$. The continuation procedure, a detailed description of which can be found in [23], consists of three steps:

1. The d_l and d_r matching values $g_1, g_2, \ldots, g_{d_l}$ and $g_{N+1-d_r}, g_{N-d_r}, \ldots, g_{N+1}$ are projected on a Gram polynomial basis.
2. Continuations to zero $g_l(x_j)$ and $g_r(x_j)$ are produced for each orthogonal polynomial at the left and right extremes of the function. These continuations extends from the d_l points and the d_r points along C extra points, and smoothly transition to zero.
3. These continuations to zero are combined to obtain the total continuation of the function, $g^c(x_j)$.

This procedure renders a smooth and periodic continuation of the original function, such that $g^c(x_j) = g(x_j)$ for $j = 1, 2, \ldots, N + 1$.

The whole continuation procedure might be expressed in matrix form as:

$$\mathbf{g}^c = \begin{bmatrix} \bar{\mathbf{I}} \\ \bar{\mathbf{A}} \end{bmatrix} \mathbf{g}, \tag{13}$$

where $\mathbf{g}^c$ is the vector of the $N + C + 1$ continued function values $[\mathbf{g}^c]_j = g^c(x_j)$, and $\bar{\mathbf{I}}$ is the identity matrix. The matrix $\bar{\mathbf{A}}$ is given by:

$$\left[\bar{\mathbf{A}}\mathbf{g}\right]_j = [\bar{\mathbf{A}}_l \bar{\mathbf{Q}}_l^T \mathbf{g}_l + \bar{\mathbf{A}}_r \bar{\mathbf{Q}}_r^T \mathbf{g}_r]_j$$
$$= g_l(x_j) + g_r(x_j). \tag{14}$$

where the columns of $\bar{\mathbf{Q}}_l$ and $\bar{\mathbf{Q}}_r$ are given by the d_l and d_r values of the Gram polynomial basis mentioned in point 1) above, and the columns of $\bar{\mathbf{A}}_l, \bar{\mathbf{A}}_r$ contain the C continuation values that blends the Gram polynomial basis to zero [25]. The number of matching points, d_l and d_r, determine the order of the approximation. For example, if $d_l = d_r = 5$, as chosen for all cases below, the Gram polynomial approximation $g^c(x)$ approximates $g(x)$ with fifth order accuracy, and the derivative dg/dx is obtained with fourth order accuracy.

The matrices $\bar{\mathbf{A}}_l, \bar{\mathbf{Q}}_l, \bar{\mathbf{A}}_r$ and $\bar{\mathbf{Q}}_r$ are obtained with high precision arithmetic in MATLAB, only once for all calculations, and then they are imported into our FORTRAN codes. A detailed explanation of the Fourier Continuation procedure, and for the construction of the matrices $\bar{\mathbf{A}}_l, \bar{\mathbf{Q}}_l, \bar{\mathbf{A}}_r$ and $\bar{\mathbf{Q}}_r$ can be found in [23–25] and references therein.

As an example, we illustrate, in Fig. 1, the cotinuation of a function $g(x) = x^{1/3}e^{\sin(x)}$, which is non periodic. The function is given between the points $x_1 = 1$ and $x_{N+1} = 5$. We choose to add $C = 25$ continuation points, setting $d_l = d_r = 5$ matching points (shown with diamonds, in the figure). The continued constructed function $g^c(x)$ is periodic. Its period b is given by the original domain of the function, plus the length of the continuation, i.e., $b = (N + C)h$. As seen in the figure, the first d_l points are replicated, by construction, exactly beyond the point $(b + 1)h$, giving rise to a periodic function. The discrete Fourier transform, determines the $N_p = N + 1 + C$
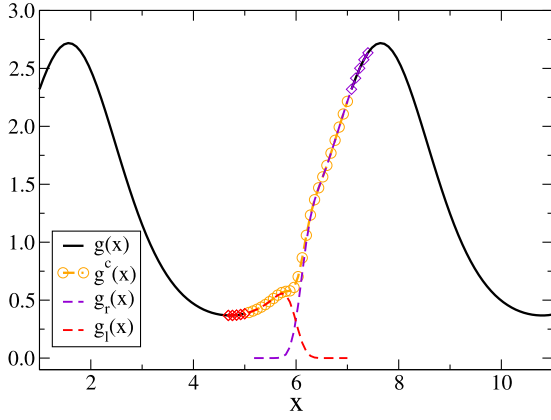
Fig. 1. Fourier Continuation of function $g(x) = x^{1/3}e^{\sin(x)}$ for $x \in [1, 5]$. The circles show the $C = 25$ continuation points, and the diamonds, the $d_l = 5$ and $d_r = 5$ matching points. The dashed curves are the continuations to zero, $g_l(x)$ and $g_r(x)$.

coefficients a_k

$$g^c(x_j) = \sum_{k=-N_p/2}^{N_p/2} a_k \exp\left(2\pi i k \frac{(x_j - x_{\min})}{b}\right), \qquad (15)$$

which allows the accurate calculation of all spatial derivatives in the advection operator of the radiative transfer Eq. (11). In order to prevent the appearance of high frequency modes which might perturb the stability of the method, an exponential filter is introduced [23]:

$$\hat{a}_k = \exp\left(-\alpha \left|\frac{2k}{N_p}\right|^{2\beta}\right) a_k, \qquad (16)$$

which is implemented, in our calculations, with $\alpha = 2$ and $\beta = 5$. The derivative is then evaluated as:

$$\frac{dg^c(x_j)}{dx} = \sum_{k=-N_p/2}^{N_p/2} \frac{2\pi i k}{b} \hat{a}_k \exp\left(2\pi i k \frac{(x_j - x_{\min})}{b}\right). \qquad (17)$$

The method shows stability under the Courant–Frederichs–Lewy condition (abbreviated as the CFL condition throughout this paper).

The algorithm to advance one time step the RTE by means of the FC–DOM approach, starting from a given initial condition, is summarized in Algorithm 1.

Algorithm 1 FC–DOM explicit scheme.

1: **for** each time–step n **do**
2:    **for** each direction $\hat{\Omega}_m$ **do**
3:      Impose boundary conditions.
4:      **for** each y **do** along x
5:        Apply Fourier Continuation $I(x, y, \hat{\Omega}_m, t^n)$.
6:        Apply FFTW to obtain Eq. (15).
7:        Apply the filter (16).
8:        Evaluate $\partial I/\partial x$ using Eq. (17).
9:      **end for**
10:      **for** each x **do** along y
11:        Steps 5-7.
12:        Evaluate $\partial I/\partial y$ using Eq. (17).
13:      **end for**
14:      Evaluate the right hand side of equation (11).
15:    **end for**
16: **end for**

---

4. Results

The present section contains four main subsections. In the first subsection we compare the accuracy and efficiency of the Fourier continuation method with a recent finite difference method (FD) proposed by Fujii et al. [26], performing a detailed error analysis. In particular, we show that our method is a fourth order approximation to the derivatives, and that the finite difference method is third order.

In the second part we construct a manufactured solution, and we compare the errors given by the FC–DOM method against the errors obtained using the finite difference method (FD–DOM) when the solution is propagated in time in two different situations.

In the third subsection we use our model for the simulation of light transport in scattering tissue. We reproduce, numerically, the experiments carried out on scattering of infrared light in tissue–like phantoms. The experiments performed by Klose et al. [19], reported detector readings (the outgoing fluence) on the boundary of the phantoms. This experiment was designed to have translational symmetry along the z direction, which makes it suitable for the 2D approximations used in this paper. We analyzed two types of these phantoms, one is homogeneous and the other contains a void–like region. This simulation tests the capability of our method to capture the physics in a real laboratory situation, where Fresnel boundary conditions are necessary. Next, in Section (4.3.3), comes a time independent benchmark used for a brief discussion on the ray effects phenomenon.

In the last subsection we validate our time dependent results introducing a problem for which the analytic solution is known. This case was published by Paasschens [31]. The analytical solution is used to validate the time numerically simulated propagation. Then we compare the performance of our FC–DOM method with the FD–DOM, using a benchmark that mimics a laboratory situation, to demonstrate the performance of both methods in realistic situations.

All simulations were run on a workstation with an AMD Ryzen 7 1700 processor with clock speed of 3.0 GHz on a Linux system. The programs were compiled using the GFORTRAN compiler.

4.1. FC Vs. FD: Error analysis

With the aim to compare our RTE results with a finite difference scheme, we implemented the spatial discretization for the advection term proposed by Fujii et al. [26], which is a third–order approximation:

$\xi_k \, \partial I_k^n / \partial x \sim$

$$\begin{cases} \frac{\xi_k}{6\Delta x}[2I_{i+1,j,k}^n + 3I_{i,j,k}^n - 6I_{i-1,j,k}^n + I_{i-2,j,k}^n] & \text{if } \xi_k \geq 0, \\ \frac{\xi_k}{6\Delta x}[-I_{i+2,j,k}^n + 6I_{i+1,j,k}^n - 3I_{i,j,k}^n - 2I_{i-1,j,k}^n] & \text{if } \xi_k < 0, \end{cases}$$

where $\xi_k = \hat{x} \cdot \hat{\Omega}_k$ is the proyection of the $\hat{\Omega}_k$ versor onto the $\hat{x}$ direction.

We compare the accuracy order for the FC and FD methods, by implementing the Fourier method and the finite differences scheme (18), for the calculation of the first derivative of a given function. We choose for the comparison, the non periodic function $g(x) = x^{1/3}e^{\sin(x)}$ for $x \in [1, 5]$, the same function that has been converted into a periodic one in the previous section. Fig. 2 shows the maximum error delivered by each method in the first derivative calculation over the whole range $\Delta g'(x) = \text{Max} |\frac{dg^n}{dx} - \frac{dg^a}{dx}|$, where g^n and g^a means the numerical and analytical functions, respectively. The maximal errors are displayed as a function of the number of points N in the numerical grid. As seen in the figure, the errors are in correspondence with the N^{-3} (for the finite differences) and N^{-4} (for FC) slopes. The Fourier continuation is a pseudospectral method, therefore, it is global in nature. In contrast, the finite
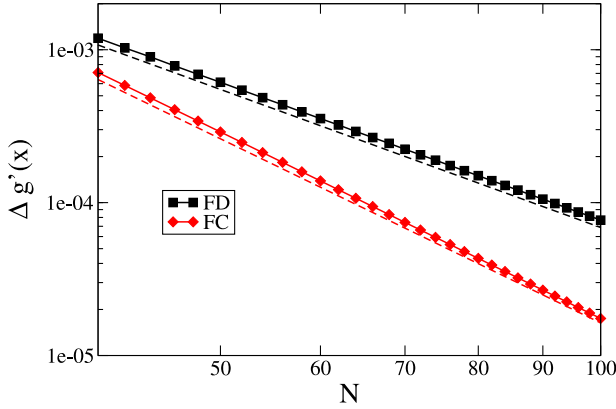
Fig. 2. Maximum error in the first derivatives of $g(x) = x^{1/3}e^{\sin(x)}$, produced by using the FC and the FD methods. The dashed lines show the N^{-3} and N^{-4} slopes.

Table 1
Phantom optical properties.

μ_s [cm^{-1}]	μ_a [cm^{-1}]	g	n_m
58	0.35	0.8	1.56

difference method, is a local method, in which the derivatives at each point are calculated using only a few neighboring points.

4.2. Manufactured solution

The first test of our FC–DOM method is performed by using a manufactured solution. That means, we propose a given analytical solution of the RTE representing the light intensity as:

$$I^a(x, y, \hat{\Omega}, t) = e^{-[x-t]^2 - [y-t]^2}$$
$$\times \{\cos(2\pi k[x + y - 2t]) + 1\}, \qquad (18)$$

which is a cosine wave having wavelength $\lambda = 1/k$, traveling along the direction $x = y$. From this intensity, we are able to calculate the analytical expression for the corresponding "manufactured source" $q(\mathbf{r}, \hat{\Omega}, t)$. The "manufactured solution" test problem then proceeds by solving the RTE equation for this source q, comparing the numerical calculated intensity I^n with the analytical solution I^a (18). The reasons for comparing fluxes rather than intensities are twofold. First, the former are in general the experimental physical observables in optical tomography, and second, they provide global information of the solutions by integrating over all the directions. Since the analytical solution is independent on the directions $\hat{\Omega}$, the analytical scalar flux is given by $\phi^a(x, y, t) = 2\pi I^a(x, y, t)$. We analyzed two different problems. The first one, corresponds to a vacuum medium, in which $\mu_s = \mu_a = 0$. In the second case, the characteristics of the diffusive media corresponds to the tissue–like phantom used in the experiments of Klose et al. [19], which is also studied in Section 4.3, and summarized in Table 1. In this table, g is the anisotropy factor that enters in Eq. (2), and n_m is the refractive index of the medium. The dimensions of the phantom are 4 length units in both the x and y directions, and we use $k = 1$.

Both the FC and FD derivative methods were incorporated into the DOM scheme, and then, into the final computational program that solves the time dependent RTE equation. For the numerical solution of these manufactured problems we use $M = 32$ discrete directions, a space interval of $dx = dy = 0.1$ and time steps with $dt = 10^{-4}$. The use of more discrete directions produced no significant effects in the global errors. Fig. 3 shows the maximum error in the fluence, $\Delta\phi(t) = \text{Max}\,|\phi^a(\mathbf{r}, t) - \phi^n(\mathbf{r}, t)|$, as a function of the time t.

There are some features to notice from these results. First, at any time, the overall error given by the FC–DOM method is smaller
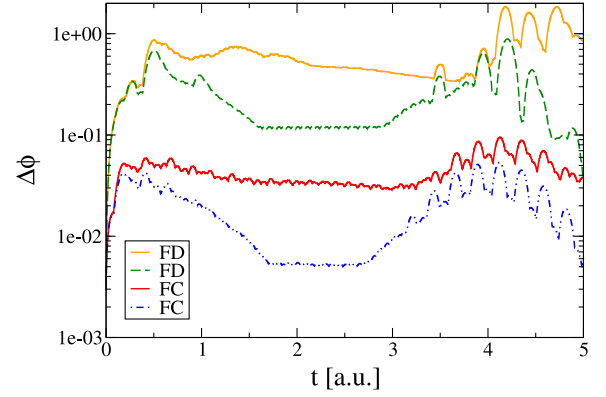

Fig. 3. Maximum error for the manufactured scalar flux (18) as a function of the evolution time. Continuous lines are for the vacuum medium, and dashed lines for the diffusive medium.

than the FD–DOM. This is consistent to the fact that FC allows the calculation of the space derivatives with much better accuracy than the finite differences method. Second, the errors in the vacuum model calculations, are higher than in the diffusive media problem. It is well known that non–scattering media require special treatments for instabilities and numerical oscillations. It is worth noting that in the FD–DOM calculations occasionally there appear unphysical negative intensities that renders the finite difference approximation unstable. In order to make the method stable, we include a fixup, replacing these negatives values by zero. Finally, the errors are higher at the initial and final times. Both methods, and specially the FD–DOM yield the higher errors at the boundary regions. The propagation in time evolves the intensity function from an initial location surrounding the origin, to regions centered at $[x - t, y - t]$. Therefore, the maximal global errors change in time, according to the intensity of the radiation at the boundaries. For the range of time in which most of the radiation is contained inside the scattering medium (2–3 a.u.), the intensity at the boundaries is negligible, and therefore, the errors are much lower.

4.3. Comparison with experimental results

This section compares results produced by our algorithm with experimental data obtained from radiation on several tissue phantoms considered in Klose et al. [19]. The measurements reported in that reference utilize phantoms composed of clear epoxy resin, with some concentration of silicon–dioxide monospheres (adjusting the scattering properties of the media), and a mixing of ink (varying the absorption properties). Since our method solves the RTE equation rather than the diffusion equation, it permits the consideration of highly scattering media that contain void–like regions (with very low absorption and scattering coefficients). We analyze two different experimental arrangements. In the first, we simulate an homogeneous rectangular cuboid. In the second experiment, the phantom also has a rectangular parallelepiped geometry, but contains inside a cylindrical ring filled with water, in order to mimic void–like regions in the tissue. In both experiments, the phantom material was illuminated by a collimated infrared laser beam ($\lambda = 678$ nm), at the midpoint of the z axis. The light fluences were measured at different positions along the x and y boundaries (illustrated by short arrows, in Fig. 4). Three sets of measurements were performed, according to the positions of the light source over the x axis (points labeled as A, B and C, in the figure).

The Fourier Continuation procedure extends the specific intensity at the boundary of the domain, allowing to treat general non–periodic boundary conditions, avoiding thus the Gibbs phe-
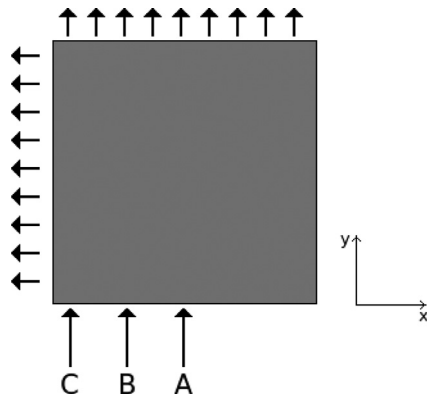
Fig. 4. Experimental setup for the three different situations. The inward arrows toward the phantom shows the three different position for the source. The outward arrows represent detector positions.

nomenona due to the non periodicity of the function. The source function and the optical parameters may also give rise to the Gibbs ringing effect if not properly treated. For that reason, the functions that approximate the source function and the optical parameters are chosen to be smooth functions. All discontinuities can thus be treated, yielding arbitrarily accurate approximations provided sufficiently sharp smooth approximations of discontinuities (together with adequately fine discretizations, which resolve the smooth approximation) are used.

Since we solve the time dependent evolution of the radiation, we evaluate the outgoing current of photons introducing a sigmoid function $T(t)$ which starts at zero and smoothly transitions to one, keeping the final solution at a numerical asymptotic time. The source function is represented by:

$$q(\mathbf{r}, \hat{\Omega}, t) = T(t) \exp \left(-\frac{|\mathbf{r} - \mathbf{r}_0|^2}{2\sigma^2} \right), \qquad (19)$$

where the spread of the beam is taken from the experiment as $\sigma = 0.1$ cm. The medium is highly scattering, therefore, all the directional initial information of the source, which might be of value in other type of experimental settings, is lost after a number of collisions a few millimeters away from the source.

We solve for a number of time steps, until the solution reaches its asymptotic behavior [32], for which $\lim_{t \to \infty} \partial I / \partial t = 0$ and then evaluate the operator of Eq. (6) along the edges where the detectors are positioned.

Once the outgoing photon current is computed, a normalization is performed in order to set the detector readings from the simulation and the one from the experiment in the same scale. For the detectors along the x axis we choose to normalize with respect to the biggest value of each curve. Results obtained along the y axis were normalized adjusting the point at the discretized grid which was found to be the closest to some of the experimental detector positions.

4.3.1. Homogeneous phantom

The first experimental arrangement reported in [19] uses an homogeneous phantom having the optical properties listed in Table 1. The size of the edges are 3 cm along the x and y axis. The sources are located at three different positions $\mathbf{r}_0$: $A = (1.5, 0)$ cm, $B = (0.9, 0)$ cm and $C = (0.3, 0)$ cm.

The fluence rates calculated via Eq. (4) are displayed in Fig. 5, for the three experimental settings, corresponding to the different positions $\mathbf{r}_0$ of the light source (A at top, B in the middle, and C at the bottom). As is noticeable in the figure, the fluence for the first case is symmetric, but the system looses this property as soon as
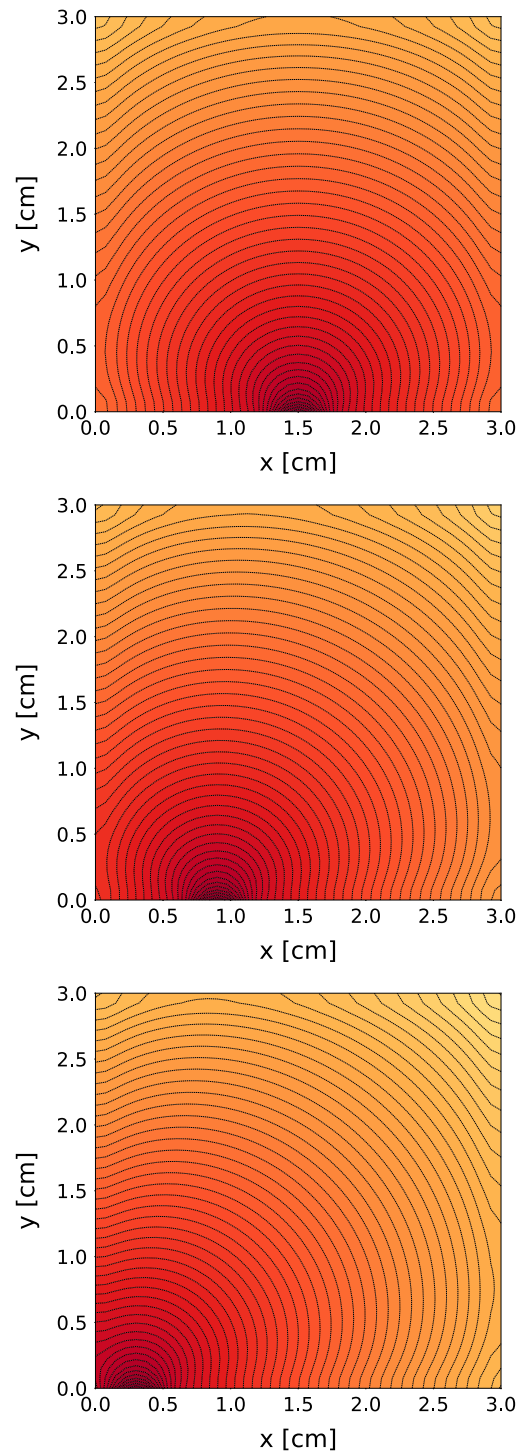

Fig. 5. (Color online). Calculated fluence rates $\phi(\mathbf{r})$ (Eq. (4)) corresponding to the homogeneous phantom simulation. The three figures display the results corresponding to a source located at A (top), B (middle) and C (botton). The results are shown in a logarithmic scale.

the source is located close to the boundary, giving rise to reflections that alter the light intensity with a particular angular dependency.

The radiation fluence of photons reaching the detectors located at the boundaries are calculated by Eq. (6). The results are shown in Fig. 6, for the 28 detectors located at the x border (top), and for the 28 y detectors (bottom). Excellent agreement is found between our simulated results (lines) and the experimental data (in sym-
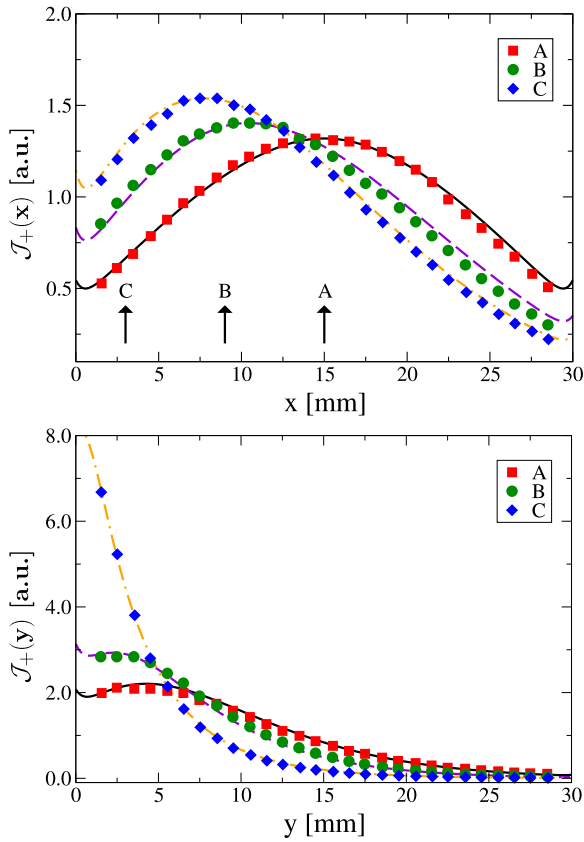
Fig. 6. (Color online). Experimental transmitted radiance measured by Klose [19] (symbols), and simulated FC–DOM results, for the homogeneous phantom (lines).

Fig. 7. Inhomogeneous phantom, with a void–like ring region in which $\mu_a = \mu_s = 0$. The scattering coefficient smoothly transitions into the void region.

bols). The maximum for the outgoing photon current $\mathcal{J}_+$ in experiments B, and specially in C, are deviated from the source position. This can be understood if one considers the radiation that is being reflected and the radiation that is escaping at the left surface. As the source gets closer to the edge, the angle from the incident radiation with respect to the normal on that surface gets bigger. Therefore, more radiation is reflected from points closer to the source, which might propagate to the right side of the media, contributing to the maximum. Contributions coming from scattered photons also are expected to be higher coming from the right, because the radiation at the left might be escaping from the media.

This experimental setting was simulated and analyzed by Klose et al. [19] in a time independent framework, by means of first order finite difference approximations to the spatial derivatives, and a Gauss–Seidel method for the matrix inversion. Those authors also considered a 2D integration, but using an extended trapezoidal rule in place of the Chebyshev quadrature used in the present work. Our numerical results and Klose's results are hardly distinguishable in the same graph.

4.3.2. Inhomogeneous phantom

The second phantom, which contains a water–filled void–filled ring, is treated in our simulations as an homogeneous body, except for the cylindrical region with diameter $d = 2.8$ cm, in which the absorption and scattering coefficients are given by $\mu_a = \mu_s = 0$. The lengths of the phantom in this experimental arrangement along x and y are 4 cm. Three experiments were simulated, according to the position $\mathbf{r}_0$ of the source, labeled $A = (2.0, 0)$ cm, $B = (1.2, 0)$ cm, and $C = (0.4, 0)$ cm. To preserve the high order of the computational method, discontinuities in the optical parameters of the medium must be avoided. Otherwise, Gibbs ringing ef-
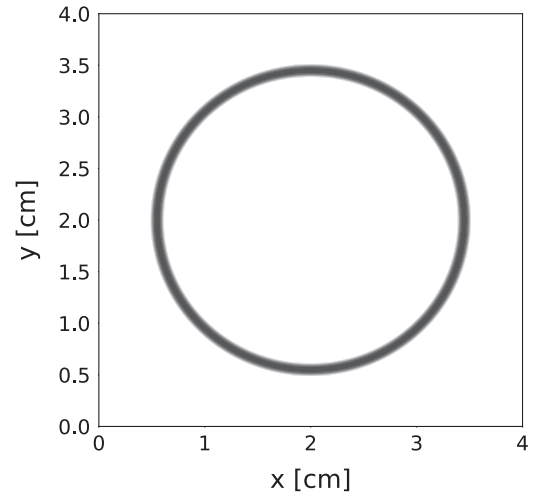
fects will deteriorate the accuracy of the calculations. For that reason, we implemented the window function introduced by Bruno et al. [33] in another context, with some slight modifications. This window function provides a smooth transition into the void region, and thus helps avoid the appearance of the Gibbs oscillations due to discontinuities in the optical parameters. A representation of the inhomogeneous phantom is given in Fig. 7, where the ring in the middle shows the void–like region.

The fluence rates calculated for the second phantom are displayed in Fig. 8. The results show overall the same characteristics as the previous calculations, but the effect of the void region is clearly noticeable. The photons are channeled inside this region, producing a feature that cannot be reproduced with the diffusion approximation.

The radiation fluence of photons reaching the 38 detectors located at the boundaries are shown in Fig. 9. A very good agreement was found between theory and experiment. The presence of void regions, like those encountered in the cerebrospinal fluid in the head, or between organs in the body –the synovial fluid in finger joints [13] or the trachea in the human neck [11]–, demands the use of transport models.

This experimental setting, as the one in the previous section, was also simulated by finite differences in a time independent framework by Klose et al. [19].

4.3.3. Ray effects

In this section we present the last time independent benchmark of this paper, which concerns an important and widely studied numerical phenomenon in the discrete–ordinates literature. We compare our FC–DOM results with a thoroughly used time independent benchmark in radiative transfer, which serves as a testbed for the well–known ray–effects phenomenon.

The ray effects phenomenon has its origin in the discretization of the angular variable $\hat{\Omega}$. The possible propagation directions in discrete ordinate methods are given by the M discrete directions $\hat{\Omega}_m$. When localized sources are present, sharp gradients in the specific intensity are originated near the source. The fluxes are only allowed to propagate in the discrete directions, giving rise to the spurious oscillations known as ray effects. We reproduce a benchmark by Crosbie and Schrenker [34], which is regarded as exact [35,36], using the method described in Section 4.3.

We consider a two dimensional square medium, of unit size, which is purely scattering with $\mu_t = \mu_s = 1$. The scattering is isotropic ($g = 0$). Uniformly over the entire bottom surface, inci-
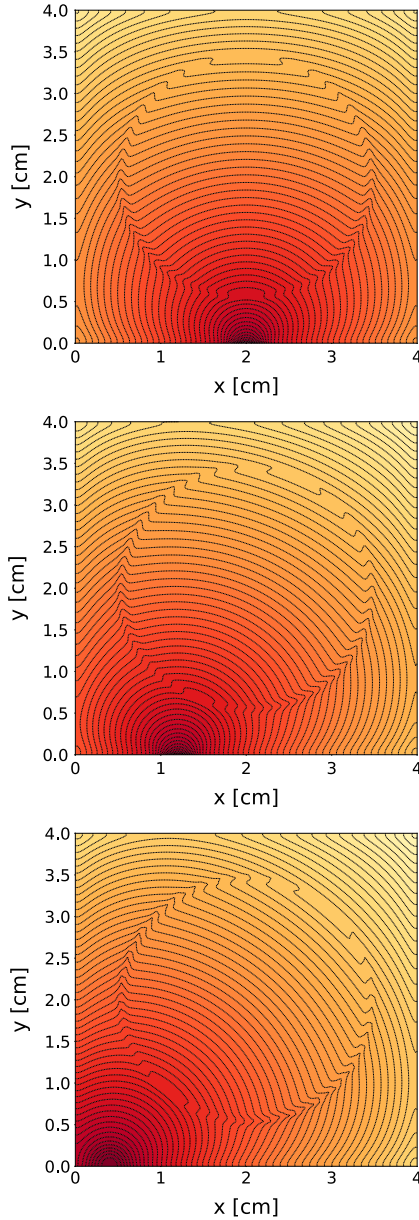
Fig. 8. (Color online). Calculated fluence rates $\phi(\mathbf{r})$ for the inhomogeneous phantom simulation.

Fig. 9. (Color online). Experimental transmitted radiance measured by Klose [19] (symbols), and simulated FC–DOM results, for the inhomogeneous phantom (lines).

Fig. 10. (Color online). Exact photon current component along the y direction, $\mathcal{J}_y(x)$ (circles), and simulated results obtained with the FC–DOM method for different number of discrete directions, M=32,64,128 (lines).

dent radiation is entering the domain. The other surfaces are subject to vacuum boundary conditions, which can be obtained by considering the indexes of refraction $n_m = n_a = 1$.

The observable considered is the y component of photon current (Eq. 5), $\mathcal{J}_y(x, y = 1)$. In Fig. 10 we present the results for this benchmark. As can be seen, ray effects are present for coarse discretizations of the angular variable, and diminishes whith increasing number of directions. Due to the fact that ray effects have its origin in the discretization of the angular variable, the FC–DOM method doesn't solve the ray effects phenomenon.

In highly scattering media, the singular behavior responsible for ray effects is rapidly attenuated away from the source, as the direct intensity responsibly for the ray effects rapidly decays [35], and radiation is redistributed in all directions. The Fourier Continuation procedure only deals with the differential operator, and has no effect in the angular discretization. Other strategies have to be considered to overcome the ray effects phenomenon when needed. Because biological tissue is a highly scattering media, in optical to-
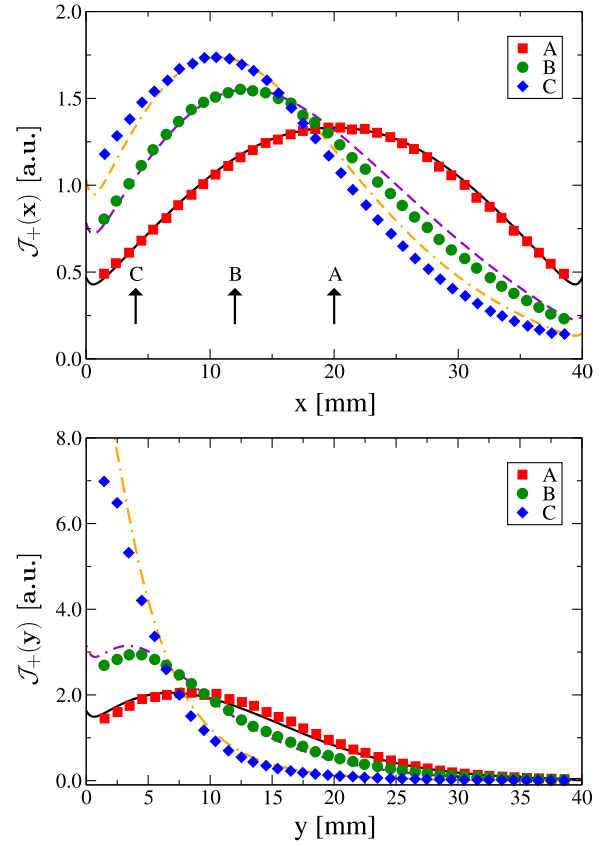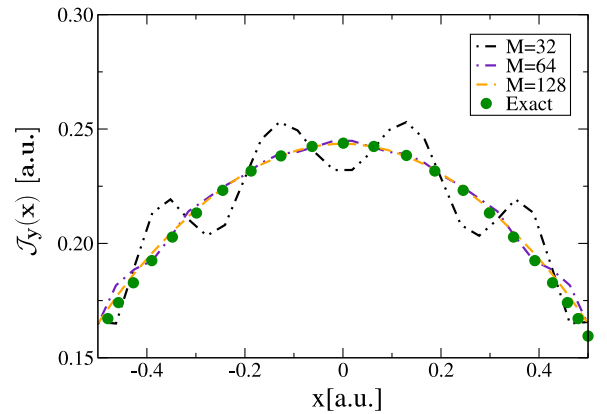
mography, the media under study is predominantly highly scattering, and in many applications ray effects are not a problem.

4.4. Comparison with an analytical solution

In this subsection we validate our time–dependent computational methods, calculating the fluence rate for an analytical problem proposed and solved by Paasschens [31]. In this problem, an infinite isotropic and homogeneous two–dimensional media is illuminated by a point–like pulse $q(\mathbf{r}, \hat{\Omega}, t) = \delta(\mathbf{r} - \mathbf{r}_0)\delta(t)$.
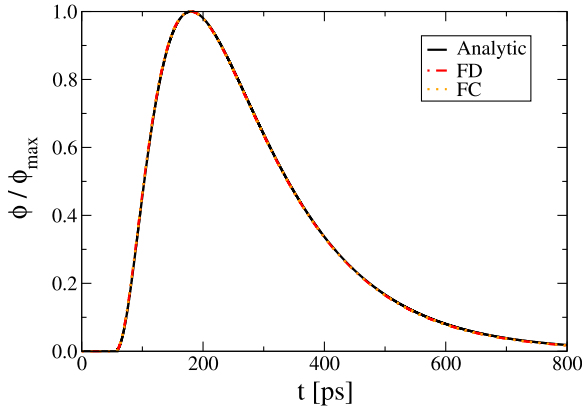
Fig. 11. Analytic solution, and numerical solutions obtained by FC–DOM and FD–DOM for an homogeneous phantom, illuminated by a point–like pulse.

The solution of this problem, is

$$\phi(r,t) = \frac{e^{-ct\,\mu_t}}{2\pi}\delta(ct-r) + \frac{\mu_s'}{2\pi ct}\left(1 - \frac{r^2}{c^2t^2}\right)^{-1/2}$$
$$\times \exp\left[\mu_s'\sqrt{c^2t^2-r^2} - ct\,\mu_t\right]H(ct-r), \qquad (20)$$

where $H(x)$ is the Heaviside step function, the parameter $\mu_s' = (1-g)\mu_s$ takes into account the anisotropy of the media, $\mu_t = \mu_a + \mu_s'$, and c is the speed of light in the medium. In the present calculation we simulate the same homogeneous phantom used in the previous calculations, with parameters $\mu_s' = 11.6/\text{cm}$, $\mu_a = 0.35$, $g = 0.8$, and a velocity $c = 0.019$ cm/ps. The first term in expression (20) represents the ballistic peak [31], raising from the unscattered photons arriving at time $t = r/c$. This feature hardly appears in numerical simulations, unless a very fine mesh is used in the calculations. Moreover, in highly scattering media, this contribution is negligible a few millimeters away from the source. In real situations the laser pulse has a finite time extent, and a Gaussian representation [37], or other kind of well behaved functions are more reliable than the Delta function.

For the numerical solution we have used vacuum boundary conditions, in which the flux entering the domain through its boundary equals zero:

$$I(\mathbf{r}_b, \hat{\Omega}, t) = 0 \quad \text{on } \Gamma_-. \qquad (21)$$

For practical purposes, in order to avoid Gibbs instabilities and a large computational effort, the Dirac delta function corresponding to the source, is approximated by a sharp Gaussian. The numerical results given by our FC–DOM calculation, together with the analytic solution (20), are shown in Fig. 11. We also include in the figure the results obtained by using the FD–DOM approach. In both cases, the agreements with the analytical result are excellent.

To give a quantitative idea of the convergence properties for both methods, we define the overall relative error with respect to the analytic solution as

$$\Delta\phi(r) = \sqrt{\frac{\int_{t_0}^{t_f} |\phi^a(r,t) - \phi^n(r,t)|^2\,dt}{\int_{t_0}^{t_f} \phi^a(r,t)^2\,dt}}, \qquad (22)$$

where $\phi^a(r,t)$ is the analytic scalar flux, and $\phi^n(r,t)$ are the fluxes obtained from the numerical simulations with the FC and FD methods. The time $t_0 = 70$ps and $t_f = 400$ps are chosen to avoid the singular behavior at $t = r/c$, and effects associated to the boundaries for the later times. In contrast to the qualitative agreement shown in Fig. 11, the errors are calculated without normalization, and instead of the Gaussian function approximation, the solution is evolved from t_0 to t_f from an initial condition given by

Table 2
Convergence to analytic scalar flux.

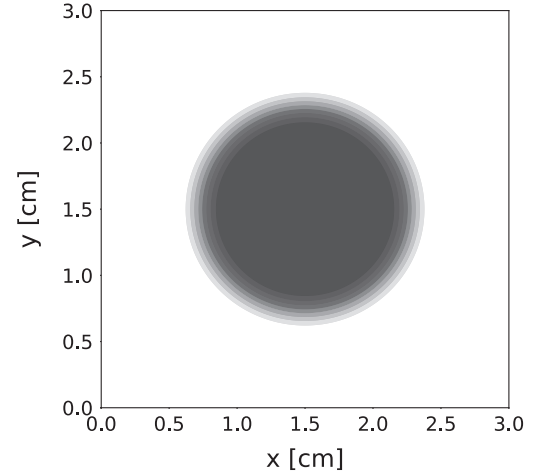| Δ	$\Delta\phi_{FC}(r)$	$\Delta\phi_{FD}(r)$
0.250	5.8×10^{-3}	1.5×10^{-1}
0.125	1.8×10^{-4}	2.2×10^{-2}
0.100	4.7×10^{-5}	1.1×10^{-2}

Fig. 12. Phantom with a void region (in dark).

the analytic solution at time t_0 (eq. (26) from reference [31]). This gives an exact approximation to the solution at $t = t_0$, and avoids numerical errors introduced in the approximation to the Dirac delta function. We consider the error for $\Delta\phi(r,t)$, with $r = 1.27$cm from the pulse. In Table 2 we show the errors associated to the FC and FD methods for simulations with $M = 16$ discrete directions, $T = 3.3 \times 10^5$ time steps and a varying number of points for the spatial coordinates, where $\Delta = \Delta x = \Delta y$.

Table 2 clearly shows that the error resulting from use of the FC method is significantly smaller than that resulting from the FD method, by orders of magnitude, for all the values of N tested.

In order to test our computational method in a situation that resembles a laboratory setting, we performed an additional simulation of a more realistic physical problem. Here, we calculate the outgoing photon flux (Eq. (6)) read at the boundary of a cuboid phantom having the same dimension ($x = y = 3$ cm), and the same optical parameters as before, but containing a fully cylindrical void region at the middle, as displayed in Fig. 12. Note that the void region in this example is a cylinder, not a cylindrical ring.

The radiation source is represented by the same Gaussian function (19), with $\sigma = 0.5$ cm, and it is placed at $\mathbf{r}_0 = (1.5, 0)$ cm. The detector is fixed at the point $\mathbf{r}_d = (1.5, 3.0)$ cm. Fresnel boundary conditions are imposed. An analytical solution is not known for this problem. Therefore, the comparisons between FC and FD calculations were performed comparing these results against a highly–refined, converged solution, which is considered as a benchmark. This reference calculation was performed with a space discretization of $dx = dy = 1.3 \times 10^{-2}$ cm. Since the length size of the phantom is 3 cm, this means that $N_x = N_y = N = 230$ grid points are utilized for the simulation. Concerning the time propagation, we used an explicit second–order Adams–Bashforth method, with a time discretization step of $dt = 10^{-3}$ ps. The propagation is carried out up to a final time of $\tau = 600$ ps utilizing $T = 6 \times 10^5$ time steps. We found convergence for $M = 32$ discrete angles $\hat{\Omega}_m$. Then, we compare the FC with the FD method, by searching for calculations producing the same error order (relative to the benchmark result). The outgoing photon currents $\mathcal{J}_+$ result-
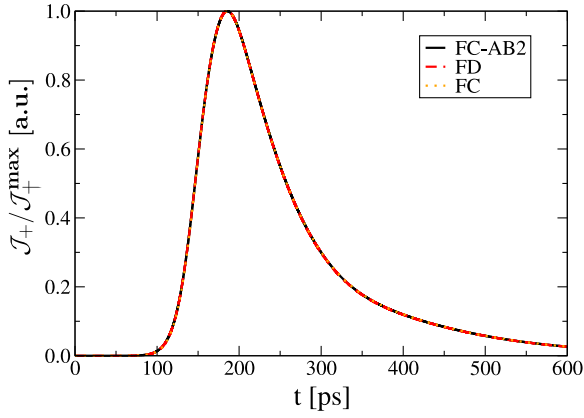
Fig. 13. Normalized outgoing photon current at the detector position for three simulations. The one taken as benchmark reference is FC–AB2.

Table 3
Convergence for $\Delta \mathcal{J}_+(\mathbf{r}_d)$.

Method	T	N	CPU time (s)	$\Delta \mathcal{J}_+$
FC	6×10^3	38	38	4.8×10^{-3}
FD	6×10^4	70	352	4.5×10^{-3}

ing from the benchmark calculation (FC–AB2), from the FC–DOM and the FD–DOM, are displayed in Fig. 13.

In order to obtain a quantitative value of the differences, we define the overall relative error as

$$\Delta \mathcal{J}_+(\mathbf{r}_d) = \sqrt{\frac{\int_0^\tau |\mathcal{J}_+^b(\mathbf{r}_d,t) - \mathcal{J}_+^n(\mathbf{r}_d,t)|^2 \, dt}{\int_0^\tau \mathcal{J}_+^b(\mathbf{r}_d,t)^2 \, dt}}, \qquad (23)$$

where $\mathcal{J}_+^b(t)$ is the reference converged benchmark solution, and $\mathcal{J}_+^n(\mathbf{r}_d,t)$ is the corresponding numerical test (FC or FD). For illustration, we analyze one set of FC and FD calculations producing the same relative errors. The sizes of both calculations, for $M = 32$ discrete directions, are summarized in Table 3.

As can be seen in the table, the finite differences method requires roughly twice the number of grid points (per dimension), and ten times the number of time steps, in order to reach the same accuracy than our Fourier Continuation method. In wall time terms, it means that the FC–DOM calculation tooks 38 seconds, while the FD–DOM tooks almost 6 minutes. For higher order methods in time, it is expected that the FC–DOM method will surpass the FD–DOM method even further.

5. Conclusions

In this work we have presented a novel approach for the treatment of the radiative transfer equation. Our method is spectral, dispersionless, and high order in the spatial variables. The proposed approach produces time resolved fluences for a given accuracy with considerable less effort than previous approaches. In contrast to diffusion approximations, the proposed approach is based on the transport equation for photons, and it therefore remains physically accurate even in presence of vacuum regions. The dispersionless property of the FC–DOM method plays a special role in vacuum media, where the transport process under the Discrete Ordinates approximation is essentially an advection problem along the discrete rays. The FC–DOM method presented here meets the accuracy and effectiveness requirements for optical tomography problems. In this work we have used an explicit Euler scheme for time propagation. Major advantages might be gained by combining the FC method with higher order methods in time.

References

[1] Chandrasekhar S. Radiative transfer. London, UK: Dover, first ed.; 1960.
[2] Dymond KF, Thonnard SE, Coy RPM, Thomas RJ. An optical remote sensing technique for determining nighttime f region electron density. Radio Sci 1997;32(5):1985–96.
[3] Qin J, Makela JJ, Kamalabadi F, Meier RR. Radiative transfer modeling of the OI 135.6 nm emission in the nighttime ionosphere. J Geophys Res A 2015;120(11):10116–35.
[4] Larsen EW. An overview of neutron transport problems and simulation techniques. In: Graziani F, editor. Computational methods in transport. Berlin, Heidelberg: Springer Berlin Heidelberg; 2006. p. 513–34.
[5] Sanchez R, Cormick NJM. A review of neutron transport approximations. Nucl Sci Eng 1982;80(4):481–535.
[6] Siegel R, Howell JR. Thermal radiation heat transfer. Third edition. New York: Taylor and Francis; 2001.
[7] Schweiger SR, Arridge Ma. Optical tomographic reconstruction in a complex head model using a priori region boundary information. Phys Med Biol 1999;44:2703–21.
[8] Wilson BC, Patterson MS. The physics, biophysics and technology of photodynamic therapy. Phys Med Biol 2008;53(9):R61–R109.
[9] Boas D, Brooks D, Miller E, Dimarzio C, Kilmer M, Gaudette R, Zhang Q. Imaging the body with diffuse optical tomography. IEEE Signal Process Mag 2001;18(6):57–75.
[10] Yodh AG, Boas DA, Pogue BW, Cerussi AE, Paulsen KD, Tromberg BJ. Assessing the future of diffuse optical imaging technologies for breast cancer management. Med Phys 2008;35(6):2443–51. Part 1
[11] Fujii H, Nadamoto K, Okawa S, Yamada Y, Watanabe M, Hoshi Y, Okada E. Numerical modeling of photon migration in human neck based on the radiative transport equation. J Appl Nonlinear Dyn 2016;5(1):117–25.
[12] Bluestone A, Abdoulaev G, Schmitz C, Barbour R, Hielscher A. Three-dimensional optical tomography of hemodynamics in the human head. Opt Express 2001;9(6):272–86.
[13] Netz U, Beuthan J, Cappius HJ. Imaging of rheumatoid arthritis in finger joints. Med Laser Appl 2001;16:306–10.
[14] Larsen EW, Thömmes G, Klar A, Seaïd M, Götz T. Simplified PN approximations to the equations of radiative heat transfer and applications. J Comput Phys 2002;183(2):652–75.
[15] Arridge SR. Optical tomography in medical imaging. Inverse Prob 1999;15:R41–93.
[16] Larsen EW. Diffusion theory as an asymptotic limit of transport theory for nearly critical systems with small mean free paths. Annal Nucl Energy 1980;7(4–5):249–55.
[17] Larsen EW, Morel JE, Miller WF. Asymptotic solutions of numerical transport problems in optically thick, diffusive regimes. J Comput Phys 1987;67(1):283–324.
[18] Fujii H, Okawa S, Yamada Y, Hoshi Y. Hybrid model of light propagation in random media based on the time-dependent radiative transfer and diffusion equations. J Quant Spectrosc Radiat Transf 2014;147:145–54.
[19] Klose AD, Netz U, Beuthan J, Hielscher AH. Optical tomography using the time-independent equation of radiative transfer part 1: forward model. J Quant Spectrosc RadiatTransf 2002;72(5):691–713.
[20] Abdoulaev GS, Hielscher AH. Three-dimensional optical tomography with the equation of radiative transfer. J Electron Imag 2003;12(4):594–601.
[21] Arridge SR, Schweiger M, Hiraoka M, Delpy DT. A finite element approach for modeling photon transport in tissue. Med. Phys. 1993;20(2):299–309.
[22] Ren K, Bal G, Hielscher AH. Frequency domain optical tomography based on the equation of radiative transfer. SIAM J Sci Comput 2006;28(4):1463–89.
[23] Albin N, Bruno OP. A spectral FC solver for the compressible Navier-Stokes equations in general domains I: explicit time-stepping. J Comput Phys 2011;230(16):6248–70.
[24] Bruno OP, Prieto A. Spatially dispersionless, unconditionally stable FC-AD solvers for variable-coefficient PDEs. J Sci Comput 2014;58(2):331–66.
[25] Amlani F, Bruno OP. An FC-based spectral solver for elastodynamic problems in general three-dimensional domains. J Comput Phys 2016;307:333–54.
[26] Fujii H, Yamada Y, Kobayashi K, Watanabe M, Hoshi Y. Modeling of light propagation in the human neck for diagnoses of thyroid cancers by diffuse optical tomography. Int J Numer Method Biomed Eng 2016;33(5):e2826.

[27] Henyey LG, Greenstein JL. Diffuse radiation in the galaxy. Astrophys J 1941;93:70–83.

[28] Kim TK, Lee H. Effect of anisotropic scattering on radiative heat transfer in two-dimensional rectangular enclosures. Int J Heat Mass Transf 1988;31(8):1711–21.

[29] Liu LH, Ruan LM, Tan HP. On the discrete ordinates method for radiative heat transfer in anisotropically scattering media. Int J Heat Mass Transf 2002;45(15):3259–62.

[30] Klose AD. Radiative transfer of luminescence light in biological tissue. In: Light scattering reviews 4. Springer Praxis Books; 2009. p. 293–345.

[31] Paasschens JC. Solution of the time-dependent Boltzmann equation. Phys Rev E - Stat Phys Plasmas Fluid Related Interdisc Topic 1997;56(1):1135–41.

[32] Bruno OP, Lyon M. High-order unconditionally stable FC-AD solvers for general smooth domains i. basic elements. J Comput Phys 2010;229(6):2009–33.

[33] Bruno OP, Delourme B. Rapidly convergent two-dimensional quasi-periodic green function throughout the spectrum-including wood anomalies. J Comput Phys 2014;262:262–90.

[34] Crosbie AL, Schrenker RG. Radiative transfer in a two-dimensional rectangular medium exposed to diffuse radiation. J Quant Spectrosc Radiat Transf 1984;31(4):339–72.

[35] Ramankutty MA, Crosbie AL. Modified discrete ordinates solution of radiative transfer in two-dimensional rectangular enclosures. J Quant Spectrosc Radiat Transf 1997;57(1):107–40.

[36] Kamdem THT. Ray effects elimination in discrete ordinates and finite volume methods. J Thermophys Heat Transf 2014;29(2):306–18.

[37] Guo Z, Aber J, Garetz BA, Kumar S. Monte carlo simulation and experiments of pulsed radiative transfer. J Quant Spectros Radiat Transf 2002;73(2–5):159–68.